Analysis of Wave-Interacting Objects in Indoor and Outdoor Environments at 142 GHz

Mar Francis De Guzman, *Graduate Student Member, IEEE*, and Katsuyuki Haneda, *Member, IEEE*

***Abstract*— In this article, an analysis of wave-object interactions is presented for an entrance hall and on a street of a residential area at 142 GHz. Single-directional channel sounding and the resulting spatiotemporal propagation path estimates are fused with the detailed geometry of the environment through a ray-launcher. The improved ray-launcher accounts for higher order reflections and realizes high correspondence of the measured paths on the geometry, allowing us to analyze wave-object interaction. In channels without line-of-sight, first- and second-order reflections contribute about 60% of the total power. Large interior and exterior walls of buildings are found most influential to the multipath channel. About half of the total received power in some links can be attributed to the reflections on small objects such as pillars and staircases in indoor and lampposts in outdoor cases. While large objects produce most of the clusters to the channel, there are links where small objects generate up to four clusters. The obtained knowledge of wave-object interaction at 142 GHz serves as guidelines to set up site-specific and geometry-based channel modeling at the frequency.**

***Index Terms*— 142 GHz, channel measurement, multipath clusters, radio propagation, ray-launching, sub-terahertz (sub-THz), wave-object interaction.**

I. Introduction

RESEARCH on the sub-terahertz (sub-THz) radio spectrum for improved communications, localization, and sensing has been growing, driven by scientific and industrial interests in the development of next-generation cellular systems [1]. While the sub-THz spectrum offers the potential for a higher data rate than any legacy cellular wireless, hardware implementation challenges such as multielement antenna arrays and high-speed samplers make its potential for commercial penetration still a valid concern and hence a research topic. Feasible transceiver designs are most likely a compromise of the hardware challenges and achievable radio link quality such as data rate, coverage, and availability. The latter is tied to wave propagation conditions at the sub-THz band, specifically 1) attenuation during wireless propagation and 2) angular and frequency selectivity of multipath components (MPCs) observed at link-ends. Studies related to the former are available for various indoor and outdoor scenarios [2], [3], [4], [5], [6], [7], and channel parameters such as the path loss model and the angular and delay spreads of the same channels considered in this study are briefly reported in [8, Sec. VI.2.1]. However, knowledge about the angular and frequency selectivity is less established because of the need for elaborated studies that are exemplified in this manuscript.

Angular and frequency selectivity of radio waves, observed at link-ends, refers to the dispersion of MPC delivering power from one link-end to another. While many representations exist to describe the selectivity, e.g., the Kronecker model [9] for the angular selectivity and the Saleh-Valenzuela model [10] for the frequency selectivity, the most versatile one would be based on relative geometries of link-ends and wave-interacting objects. Such versatile art is called geometry-based model, including widely used models such as the 3GPP [11], COST [12], and site-specific models, e.g., [13].

It may be premature to develop a geometry-based model for the sub-THz band, because of *lack of sufficient knowledge about wave-interacting objects* that produce MPCs to the radio link; it is still an open question, e.g., 1) what is a typical *material* of objects that cause meaningful power contributing to the link; 2) what is a typical *size* of meaningful objects and finally; and 3) *how much* contribution do various objects make in generating multipath clusters. While the number of MPCs and beams has been discussed at above-100-GHz band, e.g., [5], [14], [15], their understanding of the physical environment is not available. These open questions must be addressed through experiment-based studies of wave propagation. As a basic work, several studies reported isolated measurements of wave-object interaction to reveal, e.g., reflection and penetration losses at sub-THz frequencies [3], [4], [5], [7], [16], [17], [18]. More sophisticated studies as summarized in Table I identify wave-interacting objects in multipath channels in lower frequency bands [19], [20], [21], [22], [23], [24], forming a basis for the development of geometry-based channel models [12], [19], [25], [26], [27]. There is no rigorous study to identify wave-interacting objects, to the best of our knowledge, performed at sub-THz frequencies. Only a few studies discuss wave-object interaction in sub-THz channels, e.g., for an urban environment at 140.5 GHz [28], while the impact of adding reflecting objects in an office environment is studied experimentally at 145.5 GHz [5].

Manuscript received 21 March 2023; revised 14 August 2023; accepted 3 September 2023. Date of publication 29 September 2023; date of current version 20 December 2023. This work was supported in part by the European Commission through the H2020 Project ARIADNE under Agreement 871464 and through the project Hexa-X under Agreement 101015956. The work of Mar Francis De Guzman was supported by the Advanced Science and Technology Institute, Department of Science and Technology, Philippines, through the Department of Science and Technology, Science Education Institute of the Philippines. *(Corresponding author: Mar Francis De Guzman.)*

The authors are with the Department of Electronics and Nanoengineering, Aalto University, 02150 Espoo, Finland (e-mail: francis.deguzman@aalto.fi; katsuyuki.haneda@aalto.fi).

Color versions of one or more figures in this article are available at https://doi.org/10.1109/TAP.2023.3318861.

Digital Object Identifier 10.1109/TAP.2023.3318861

TABLE I
STUDIES ON IDENTIFICATION OF WAVE-INTERACTING OBJECTS

Reference	Frequency (GHz)	Scenario	Findings
[19]	0.3	Suburban	In scenarios with multiple propagation links, there can be shared scatterers across the links, indicating the physical presence of common clusters.
[20]	3.35	Urban microcell	Metallic objects with dimensions of several tens of wavelengths, such as signboards, lampposts, traffic signs, traffic lights, electricity cable boxes, and vending machines contribute significantly to the received power.
[21]	4 and 14	Outdoor-to-indoor	Interior walls of the building contribute to twice as received powers as walls of other buildings. Distant buildings can account for up to half of the received power.
[22]	5.3	Indoor hall	LOS or obstructed LOS, single, double, and triple bounce reflections from walls and ground are the dominant propagation mechanisms.
[23]	11	Indoor hall	LOS, and single-bounce reflection from the concrete wall, glass window, window frames, and pillars have a significant contribution to the received power.
[24]	32	Urban microcell	Building walls and windows, and ground contribute significantly to the received power. Small objects such as publicity boards, signboards, and lamp posts can also deliver non-negligible power.
[28]	140.5	Urban	Reflections on pillars and building walls have power levels comparable to the LOS power. Objects other than building structures, such as vegetation, are not significant reflectors.
[5]	145.5	Office	Adding reflecting objects increases the MPC powers (up to $\sim$ 6 dB for outdoor case and $\sim$ 4 dB for indoor case) and the angular diversity.

The present analysis classifies the wave-interacting objects into two types, i.e., 1) all-the-time visible large objects and 2) limited-time visible small objects. Some of these small objects are considered landmark-type objects. There are two reasons for this classification: 1) their difference in *power contributions* to the radio channel and 2) their difference in *visibility and dynamics* as a link end changes their locations. While none of the existing channel models distinguish them, the benefit of analyzing them separately becomes clear at sub-THz where many physical objects become electrically large. In radio localization studies, large planar structures can usually be exploited as virtual anchors [29]. While locally visible fixed objects, such as landmarks, allow rough localization of mobile users similar to us finding a present location by recognizing a tall tower in a street canyon.

In light of the mentioned unsolved research questions, the major contributions of the present work are threefold:

1) improving the already reported measurement-based ray-launcher (MBRL) to analyze wave-interacting objects up to higher order reflections at 142 GHz in indoor and outdoor sites;
2) analyzing properties of the wave-object interaction separately for all-the-time visible large objects and limited-time visible small objects for the first time in the literature; and finally,
3) understanding the identified large and small wave-interacting objects through multipath clusters that are popularly discussed in geometry-based stochastic channel models.

The remainder of this article is organized as follows. Section II discusses enhancements and evaluation of the MBRL to identify wave-interacting objects. Section III introduces radio channel measurements in indoor and outdoor scenarios. After detailing the characteristics of identified wave-interacting objects in Section IV, conclusion is given in Section V.

II. IMPROVED MBRL

An MBRL is a tool to determine the actual trajectory of the MPCs extracted from the measurements. Such a tool is referred to as channel transfer function reconstruction in [23], measurement-based ray-tracer in [22], and MBRL in [30]. In the present study, given the single-directional channel measurements, the tool allows us to derive the location of the wave-interacting points and the angular information such as the azimuth and zenith angles of arrival (AoA and ZoA) and the azimuth and zenith angles of departure (AoD and ZoD) leading to the double-directional information of the channel. It is similar to ordinal ray-launching where rays are launched along a trajectory until they interact with an object and then undergo reflection, scattering, diffraction, and transmission. The differences are: 1) the MBRL launches the ray only in the directions where multipath was observed in measurements and 2) the ray length of a launched ray in the measured direction corresponds to its measured propagation delay.

A previous version of this MBRL is described in [31], which can estimate MPC trajectories of up to second-order reflections only. While the MBRL used here allows tracing up to fourth-order reflections to gain more understanding of wave-interacting objects. The following sections describe the implementation of the enhanced MBRL.

A. Point Cloud Data Processing

The digital 3-D map used in this MBRL is a point cloud data which is a collection of (x, y, z) point coordinates retrieved from laser scanning. These point cloud data are typically converted into a surface model called mesh to represent the environment. However, conversion from point cloud to mesh is not straightforward and some details of the environment

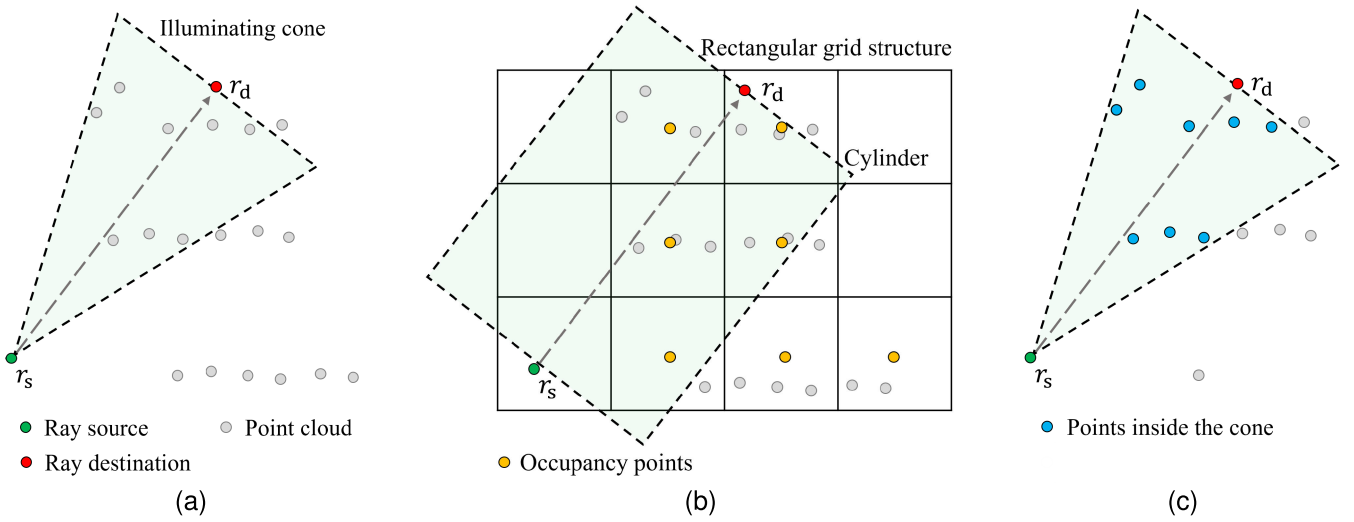

Fig. 1. Determining points illuminated by a cone. (a) Illuminating cone. (b) Grid structure, occupancy points, and in-cylinder test. (c) Identified points using the in-cone test.

are lost in the mesh model. The importance of retaining these small details for propagation simulations is also emphasized in [32]. Hence, the developed MBRL readily accepts point cloud data without the need to apply mesh conversion.

Additional processing of the raw point cloud data includes downsampling using a box grid filter with a specified grid step which we refer to in this article as the *point cloud resolution*. The point cloud data are downsampled to 4 cm for the indoor environment and 8 cm for the outdoor environments which should be enough to represent small details and allow MBRL to run in a reasonable time. Further preprocessing steps applied to the point cloud data include: 1) removal of artifacts resulting from moving objects during laser scanning; 2) elimination of noise points; 3) filling of holes caused by transparent objects and other objects shadowed during the laser scanning; and 4) derivation of local surface normals.

No additional remodeling is applied to posts, trees, and other small objects. All objects in the point cloud data are modeled as obtained from the laser scanning of the environment. While a cylinder-like geometry can be their simpler model that may expedite the calculation of reflected rays, our MBRL simulation focuses on the accurate identification of rays by avoiding remodeling.

B. Illuminating Cone

In the previous version of the MBRL [31], rays had a fixed radius which could miss objects that could have otherwise been illuminated. Due to the simulation speedup gained from the use of voxel traversal, discussed in Section II-C, an illuminating cone that can cover a larger area is now implemented and is elaborated in this section.

An illuminating cone with its vertex at the Rx location and cone opening pointed to the direction of the measured AoA is used to identify points illuminated by the Rx Antenna as shown in Fig. 1(a). The opening angle of the cone is set to be equal to the azimuth scanning step of the horn antenna in channel sounding, i.e., 10°, and the diameter of the base of the cone is a function of the measured path delay. The point cloud contains millions of points so checking whether each point is inside the illuminating cone is computationally heavy. We applied here a multistep in-cone test that utilizes a rectangular grid structure to speed up this process as follows.

1) A 3-D rectangular grid structure with a grid step that is ten times larger than the point cloud resolution is formed. Then, a so-called occupancy point is placed at the center of boxes that contain at least one point as shown in Fig. 1(b). These occupancy points provide a coarse representation of the point cloud with significantly less number of points than the point cloud data.
2) Then, only the boxes with occupancy points found inside the cylinder are considered for the succeeding steps as shown in Fig. 1(b). This cylinder has the same position and orientation, and a slightly larger diameter than that of the illuminating cone. A cylinder is applied for now as the in-cylinder test is computationally lighter than the in-cone test.
3) Finally, the in-cone test is applied to the member points of occupied boxes found in Step 2 to determine points inside the illuminating cone as shown in Fig. 1(c).

As the directional antenna illuminates the environment at the measured AoA with some beamwidth in the azimuth and the elevation, the MBRL should ideally launch rays from Rx to all the points illuminated by the main lobe of the antenna. This can be addressed by applying the illuminating cone described above to the directions not only at the exact measured azimuth but also at the neighboring directions [31].

C. Visibility Check Using Voxel Traversal

Among the points identified inside the illuminating cone, only the points visible from Rx should be considered for the reflection. We detect if the ray is obstructed by an object by applying a ray-plane intersection test. Here, we form these planes by treating the points in the point cloud as disks [33]. The orientation of the disk is equal to the normal calculated in Section II-A. We set the radius by heuristic means to be $1.1\times$ larger than the point cloud resolution.

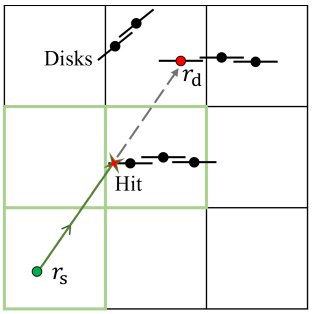

Fig. 2. Visualization of voxel traversal in a 2-D grid of disks.

This visibility check is applied numerous times during the ray-launching process making it responsible for most of the simulation runtime. A brute-force approach, used in the previous version of the MBRL [31], is to check the visibility of a particular disk by applying a ray-disk intersection test across all the disks in the scene and the disk with the shortest distance from the ray source corresponds to the visible disk. Here, we implemented the fast voxel traversal algorithm [34] to check the visibility of a disk from a ray source, such as the Rx antenna or a reflection point. As shown in Fig. 2, the grid is incrementally traversed from the ray source and stops when either it hits a disk or it reaches the ray destination. This way, the ray-disk intersection test is applied significantly less number of times compared to the previous version [31].

III. Radio Channel Measurements

A. Channel Sounder

Radio channel measurements were performed using a Vector Network Analyzer (VNA)-based channel sounder [35]. It integrates frequency converters to translate the intermediate frequency in the VNA to radio frequency (RF) from 140 to 144 GHz. With 10 001 frequency sweep points, the sounder has a delay resolution of 0.25 ns and a maximum measurable path delay of 500 m, accounting for the inherent delay of the sounder. The IF and local oscillator signals are shared between the two sides of link ends through a radio-over-fiber system which has electrical-to-optical and optical-to-electrical converters, and a military-grade optical fiber cable with two single-mode fibers to enable long-range measurements.

The Tx side of the channel sounder has 0 dBi vertically-polarized omnidirectional bicone antenna with 45° elevation half power beamwidth (HPBW), while the Rx side has 19 dBi vertically-polarized horn antenna with 10° azimuth HPBW and 40° elevation HPBW mounted on a rotator. This configuration allows directionally resolved measurements only on the Rx side. The rotator was set to sweep the azimuth angles with a 5° step while the main beam of the antenna is fixed at the horizontal plane. The height of the Tx and Rx antenna is set to 1.85 m. With effective isotropic radiated power of 30 dBm, observed noise floor of −128 dBm, and assumed margin of 10 dB, the measurable path loss of the channel sounder is 148 dB.

TABLE II
Measurement Campaign Details

Environment	Entrance hall	Residential area
Scenario	Indoor hall	Urban micro
Number of LOS Links	28	23
Number of NLOS Links	47	37
Link Distance Range (m)	3 - 66	20-175

B. Channel Sounding

Two measurement scenarios were considered in this study. The first one is in the entrance hall of a modern office building. It is an indoor space with roughly 80 × 30 m floor area in which most have high ceilings and some have first-floor ceilings. The majority of the space is an open hallway while some parts are occupied by staircases, chairs, tables, front desk, and other objects. The second measurement campaign was performed in a street residential area. The street is mostly surrounded by apartment buildings and some commercial buildings. The measurement floor plan of the two scenarios is shown in Figs. 3 and 4, respectively. The number of LOS and NLOS links and link distance range for each environment are summarized in Table II.

Measurements of a single Tx–Rx link provide a power-angular delay profile (PADP) that gives the received signal intensity as a function of the propagation delay and AoA. Local peak search of the PADP is applied to identify the propagation paths [36], [37]. The peaks obtained from this process provide a discrete representation of the multipath channel denoted by $P = \{\phi_n, \tau_n, G_n\}$, where ϕ_n is the azimuth angle-of-arrival, τ_n is the delay, and G_n is the gain of the nth path.

IV. Characteristics of Wave-Interacting Objects

The wave-interacting points identified using MBRL are further analyzed in this section.

A. Path Mapping Rate

The efficacy of this MBRL is evaluated by comparing the totality of paths that were successfully mapped on the geometry of the measurement site to that of measured paths [31]. The average portion of measured paths in each link that were successfully mapped on the geometry is 85%, and the average power percentage of successfully mapped paths is 88%.

B. Power Share Based on Order of Reflections

The power share of the traversed paths relative to the total received power of all the measured paths in LOS and NLOS links in terms of the order of reflections and missed paths are shown in Fig. 5. For LOS links, around 80% of the power comes from the direct path, and the remaining power mostly comes from reflections of the first and second order. In the case of NLOS links, first and second-order reflections constitute approximately 60% of the total power, while most of the

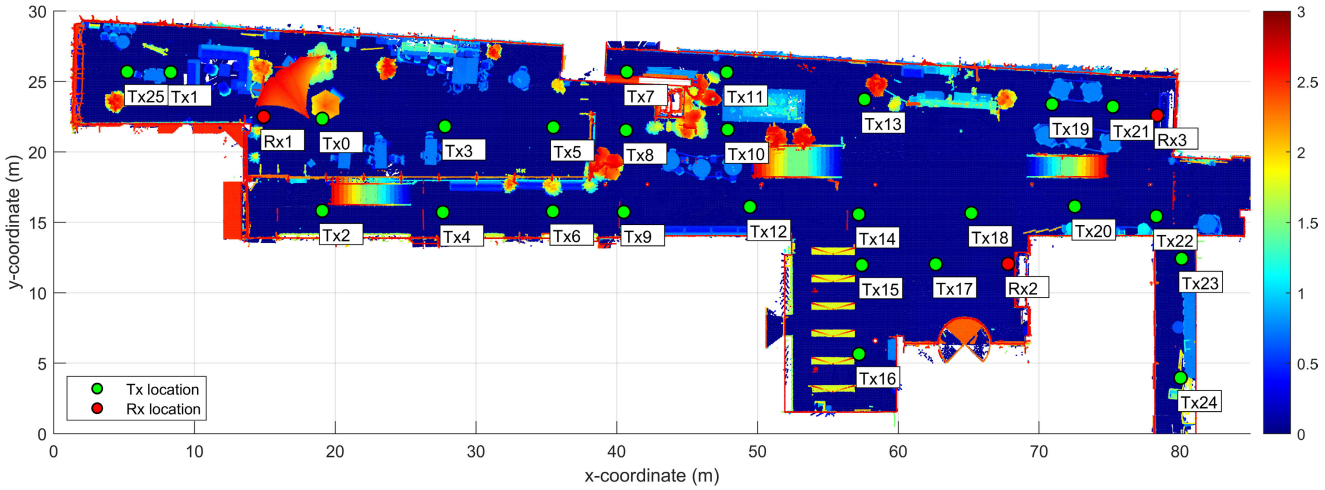

Fig. 3. Top view of the point cloud map of the entrance hall with the antenna locations.

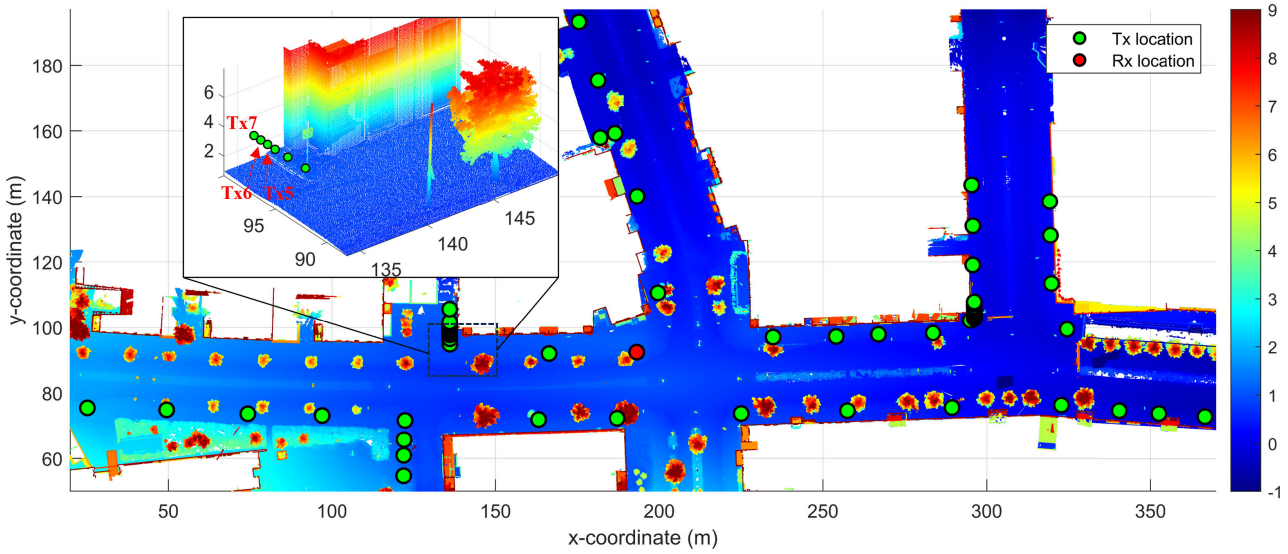

Fig. 4. Top view of the point cloud map of the residential environment with the antenna locations and zoomed-in view portion of the map.

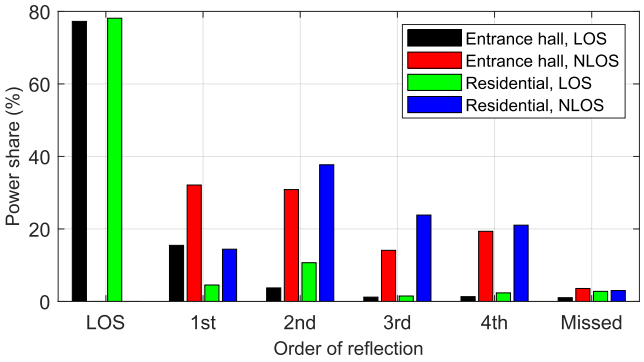

Fig. 5. Power contribution of each order of reflection in the entrance hall and residential environments.

remaining power still originates from third- and fourth-order reflections.

Fourth-order reflections occur when the ray coincidentally interacts with highly reflective materials such as metals. An example trajectory of a path with fourth-order reflections, observed in the Tx3–Rx1 link of the entrance hall case, is shown in Fig. 6. It interacts with three metal and one glass surface. The measured excess loss of the path is 20 dB as shown by the difference between the free space path gain and the gain of path 4 in Fig. 7. This value is reasonable considering that metallic surfaces generally have low reflection loss and the glass surface has a typical reflection loss of 10 dB, as will be discussed in Section IV-E and reported in Table III.

Missed paths are those that the MBRL was unable to map onto the geometry successfully, which could be attributed to potential inconsistencies between the measured and actual geometries of the environment. They may also result from unaccounted propagation mechanisms, such as transmission and diffraction, that may occur in certain paths. An example illustrating diffraction can be seen in the Tx5–Rx link within the residential scenario, where Tx5 is positioned behind the building as shown in Fig. 4. Its channel impulse response at the direction of the building corner is shown in Fig. 8(a) revealing a path that has a delay close to that of the diffracted path delay according to the relative geometry of the Tx5, building

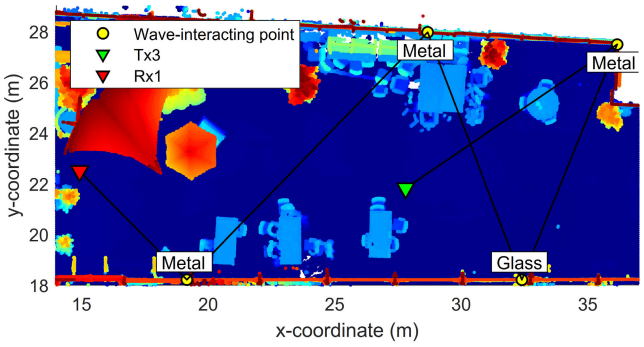

Fig. 6. Trajectory of a path in the Tx3–Rx1 link within the entrance hall scenario with fourth-order reflections.

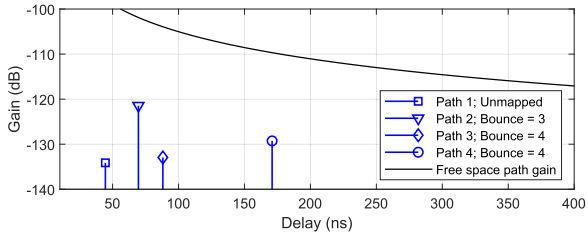

Fig. 7. Channel impulse response at the direction of the bottom metallic wall of Tx3–Rx1 link in the entrance hall scenario.

corner, and Rx. The diffraction loss, estimated by subtracting the path gain from the free space path gain, is 11 dB while its diffraction angle is 6°. No diffracted path is observed for the deeper nonline-of-sight Tx locations behind the building starting from Tx6 which has a diffraction angle of 15° as shown in its channel impulse response in Fig. 8(b). This demonstrates the significance of diffraction up to some extent, hence its inclusion in the MBRL will be considered in future work.

Accounting for transmission and diffraction is more crucial at lower frequencies to achieve a higher mapping rate using the MBRL. This leads to a significant increase in simulation time, as each interaction of a ray with an RF-transparent object or a diffracting edge would generate not only reflected rays but also transmitted and large number of diffracted rays. Reduction of the point cloud resolution or exclusion of small details from the point cloud model must also be considered. Checking wave-object interaction for diffraction on and transmission through these details is computationally very costly and hence is an implementation challenge.

C. Classification of Wave-Interacting Objects

The wave-interacting objects are classified into two main groups, namely, 1) large and 2) small objects. Large objects are those structures that span the whole environment making them visible to almost every antenna location. Some examples of these objects are walls, floors, and ceilings. Reflection points of MPCs identified on the wall in the entrance hall are shown in Fig. 9.

On the other hand, small objects are visible only within a small region of the environment. Reflection points of MPCs found on these small objects in the entrance hall are shown in Fig. 10. Unclassified points are those that are either outliers

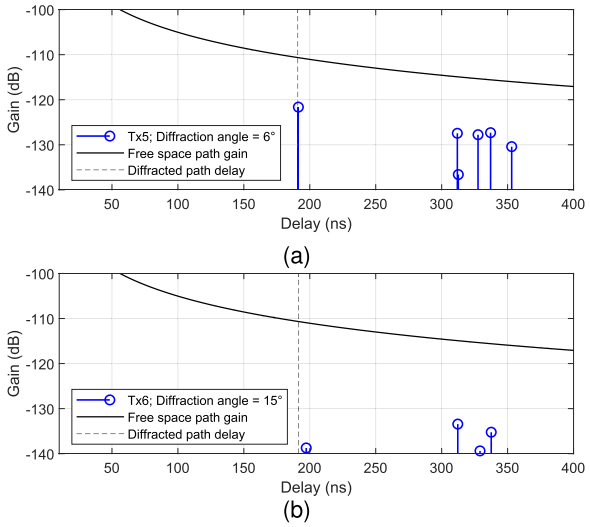

Fig. 8. Channel impulse response at the direction of the building corner of the residential environment of links (a) Tx5–Rx, with diffracted path observed and (b) Tx6–Rx with no diffracted path observed. The two Tx locations are separated by 0.65 m.

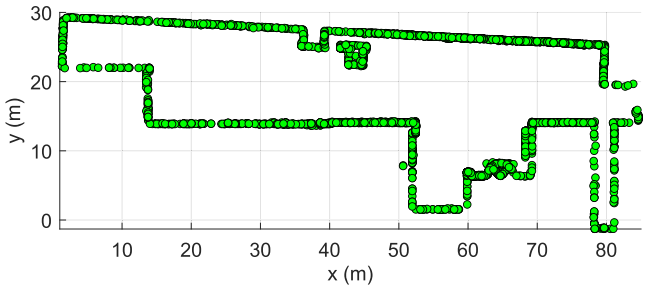

Fig. 9. Wave-interacting points identified on the wall of the entrance hall.

or combinations of different objects that cannot be separated into different objects. The classified large and small objects and their typical material composition for the entrance hall and residential scenario are listed in Tables III and IV, respectively.

D. Power Share of Each Object

To measure the impact of these identified objects on the radio channel, their power share is derived. It is defined here as the power contribution of all the wave-interacting points on an object over the total power received in a link and is calculated as

$$P_{\mathrm{S}} = \frac{\sum_{i=1}^{N_s} P_i^{\mathrm{p}}}{P_{\mathrm{tot}}} \tag{1}$$

where P_i^{p} is the power contribution of ith wave-interacting point and N_s is the number of wave-interacting points on an object. P_{tot} is the total received power without the line-of-sight path contribution. It is assumed here that the path power that undergoes multiple interactions is shared among multiple wave-interacting objects, as

$$P_i^{\mathrm{p}} = \frac{10^{\frac{-G|_{\mathrm{dB}}}{10}}}{N_{\mathrm{B}}} \tag{2}$$

where G is the measured gain of the path where the ith wave-interacting point contributes; the notation $\{\cdot\}|_{\mathrm{dB}}$ means

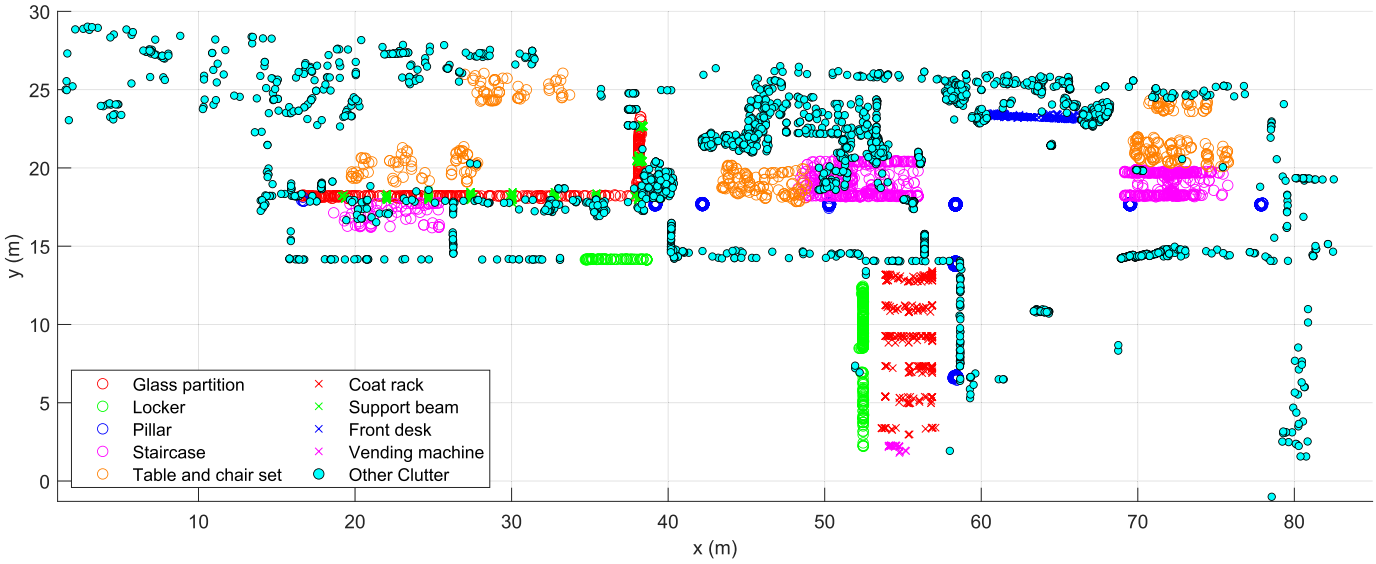

Fig. 10. Wave-interacting points identified on various small objects of the entrance hall.

TABLE III
CHARACTERISTICS OF WAVE-INTERACTING OBJECTS IN THE ENTRANCE HALL

	Object	Material	Structure	$P_S(\%)$		L_R (dB)		N_{SB}	d_{max} (m)	N_{CO}	
				Med	Max	Med	Min			Med	Max
Large	Wall	Metal, concrete, glass, and wood	Vertical planar structures of varying materials that surround the environment.	30	98	22	0	79	>45	3.9	10.9
	Floor	Granite	Single flat floor.	11	46	18	8	13	>45	1.0	3.3
	Ceiling	Plasterboard and concrete	3.3 m high first-floor ceiling that covers around one-third of the area. Painted with textured paint.	3	58	20	7	5	>45	0.5	4.5
Small	Glass partition	Glass	4 m high glass partitions.	1	89	10	4	9	40	0	4.9
	Locker	Metal	5 m wide and 1.5 m high metallic lockers with grooves.	1	29	19	19	3	44	0	1.1
	Pillar	Metal	3.3 m high and 0.5 m diameter cylindrical pillars.	2	50	20	14	31	36	0.4	4.2
	Stair	Wood and glass	3.3 m high staircase with wooden tread and handrail, and railing with glass panel and metallic brackets.	3	62	26	6	18	45	0.5	3
	Table chair set	Wood	Set of wooden tables and chairs.	1	50	25	25	2	41	0.2	1.5
	Coat rack	Metal	Metallic coat rack hanging from the ceiling.	0	8	35	35	1	20	0	2.3
	Support beam	Metal	4 m high metallic beam that supports the glass partition.	1	49	33	33	1	46	0.1	2.1
	Front desk	Granite	6 m wide and 1.5 m high front desk.	0	9	N/A	N/A	0	19	0	1.1
	Vending machine	Metal	1 m wide and 2 m high vending machine.	0	1	N/A	N/A	0	32	0	0.6
	Other clutter	Various materials	Tables, couches, LCD screen, signages, decorations, etc.	14	85	27	3	43	N/A	1.9	5.8

a quantity of $\{\cdot\}$ in the decibel scale; N_B is the number of bounces occurred in the path.

The median (med) and maximum (max) power share estimates of each object across all links where they contribute to the entrance hall are listed in Table III. For large objects, the wall gives the highest median power share followed by the floor and then by the ceiling. The ceiling has a smaller median contribution compared to the floor, due to its smaller surface

TABLE IV
CHARACTERISTICS OF WAVE-INTERACTING OBJECTS IN THE RESIDENTIAL SCENARIO

Object		Material	Structure	$P_S(\%)$		L_R (dB)		N_{SB}	d_{max} (m)	N_{CO}	
				Med	Max	Med	Min			Med	Max
Large	Wall	Concrete, brick, metal, glass.	Exterior wall of the building including other vertical planar structures such as doors and windows.	45	100	22	5	20	>170	0.8	5
	Ground	Concrete and asphalt	Outdoor ground which is mostly road and sidewalk.	23	87	4	0	2	>170	0.5	2.4
Small	Posts	Metal	Outdoor building pillars, street light posts, and traffic sign posts.	4	75	30	20	5	146	0.3	1.5
	Other clutter	Various materials	Tree trunk, bicycle parking rack, railings, plant box, bench, etc.	31	97	12	0	14	N/A	0.7	4.8

area and higher surface roughness. Nonetheless, these power share results for floor and ceiling support the importance of using a 3-D representation of the environment in simulations and channel models. As for the small objects, while their median power share is minimal, some have a high maximum power share for specific links. For example, pillars have 2% median power share but there is a particular link where its power share can reach up to 50%. In addition, coat rack which has irregular and generally thin parts have a considerable contribution that can reach up to 8% to a certain link.

The power share of objects in the residential scenario is listed in Table IV. Similar to the entrance hall, most of the power is due to building walls followed by the ground. Reflection on posts can also contribute significantly to the received power on a link.

E. Reflection Loss

The interaction of the electromagnetic waves with an object can be quantified by the object's reflection loss which depends on the angle of incidence, material thickness and composition, and surface roughness. From the MBRL-derived multipath data, we have identified single-bounce multipaths with which we estimate the reflection loss of each single-bounce wave-interacting point, without knowing the exact material properties, as

$$L_{R,i}|_{dB} = -G_i|_{dB} - 20\log_{10}(4\pi\tau_i f) \tag{3}$$

where G_i is the measured gain and τ_i is the measured path delay of ith single-bounce path.

The median and minimum reflection loss of objects, and the number of single-bounce wave-interacting points N_{SB} for each object in the entrance hall are summarized in Table III. Among the large objects, it can be noticed that the floor has the lowest median reflection loss. The wall is a mix of objects with various material compositions and shapes, and the ceiling has some roughness due to the textured paint applied on its surface. The reflection loss of the wall can reach as low as 0 dB which is caused by some flat metallic objects. For the small objects, the glass partition which is a smooth planar object has the lowest median loss and minimum loss. Meanwhile, although the locker and pillar are metallic, they have some amount of loss since their structure is not planar. Furthermore, ceiling-mounted coat racks, and support beams which are also metallic have even higher reflection loss and both of them have only one single-bounce wave-interacting point as their structure is more complex and more irregular. Note that there is no reflection loss estimate for the front desk and vending machine because there is no single-bounce reflection identified on those objects.

The reflection loss and the number of single-bounce MPCs for the residential scenario are listed in Table IV. The typical reflection loss of MPCs on the wall for this scenario is found to be the same as the entrance hall. As for the ground, the computed reflection loss may not be as meaningful as other objects since there are only two single-bounce MPCs found on this object. This can be explained by considering first that single-bounce ground reflection is likely to occur only on LOS links. However, since the antenna height is significantly small relative to the link distances available in this scenario, the ground-reflected path cannot be distinguished from the LOS path which has almost equal path delay. It can also be noticed that the reflection loss due to posts is higher compared to the pillars in the entrance hall which has the same cylindrical shape but with larger diameter.

F. Object Visibility Distance

We further describe the influence of each object on the radio channel by the object's visibility to Tx or Rx antenna locations. To this end, the distance between the wave-interacting objects and the Tx and Rx antennas is evaluated. The furthest distance d_{max} that each object is seen from the antenna locations is considered as its visibility distance as shown in Fig. 11. The visibility distance for the entrance hall and residential scenario are summarized in Tables III and IV, respectively. It can be noticed that there is no strong correlation between the reflection loss and the maximum distance parameters. This is because the object's visibility depends more on its height than size. Objects that are tall or at elevated locations such as support beams and staircases show larger visibility distances than those that are small and/or on the floor, e.g., coat rack

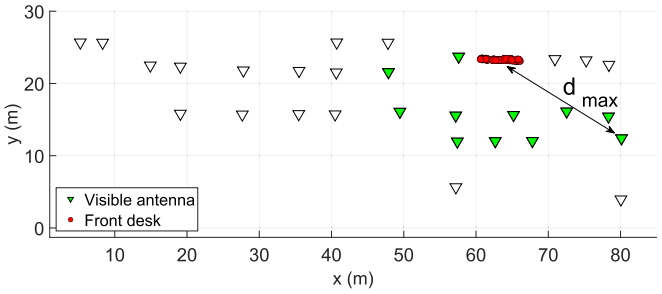

Fig. 11. Visibility distance of front desk in the entrance hall.

and front desk. Identification of influential wave-interacting objects therefore requires 3-D studies.

G. Number of Clusters on an Object

The relationship between wave-interacting objects and multipath clusters is studied. Measured multipaths were clustered by applying the agglomerative hierarchical clustering method which is elaborated in [37]. Here, we performed multidimensional clustering including the azimuth and elevation angles of arrival and departure, and path delay. The multipath component distance (MCD) between two clusters c_i and c_j is then calculated as

$$\mathrm{MCD}_{ij} = \sqrt{\mathrm{MCD}_{\mathrm{A,ij}}^2 + \mathrm{MCD}_{\mathrm{D,ij}}^2 + \mathrm{MCD}_{\tau,ij}^2} \tag{4}$$

where $\mathrm{MCD}_{\mathrm{A,ij}}$ is the normalized angle of arrival, $\mathrm{MCD}_{\mathrm{A,ij}}$ is the normalized angle of departure, and $\mathrm{MCD}_{\tau,ij}$ is the normalized delay between the two clusters [38]. The clustering parameters, i.e., delay scaling factor ξ and the MCD clustering threshold Γ were heuristically determined and are set to 10 and 0.8, respectively.

The number of clusters N_{CO} on an object is defined here as the total fractional count of clusters belonging to the object in a link and can be expressed as

$$N_{\mathrm{CO}} = \sum_{i=1}^{N_{\mathrm{C}}} \frac{N_i^{\mathrm{SO}}}{N_i^{\mathrm{SC}}} \tag{5}$$

where N_i^{SO} is the number of wave-interacting points attributed to the object and ith cluster, N_i^{SC} is the number of scattering points belonging to ith cluster, and N_{C} is the number of clusters in the particular link.

The median and maximum N_{CO} across all the links for the entrance hall are listed in Table III. It can be observed that a greater number of clusters tends to form on large objects. Meanwhile, typically only half of the cluster is formed on small objects but the $\max(N_{\mathrm{CO}})$ indicates that there is a link where multiple clusters can be formed on a small object.

Table IV summarizes the number of clusters observed on objects in the residential scenario. Compared to the entrance hall, the residential scenario generally has fewer clusters, although large objects still tend to have more clusters than small posts.

H. Number of Clusters and Objects

The statistics of the number of clusters N_{C} in the two environments and other studies [14], [39] at 142 GHz are summarized in Table V. The number of observed clusters in this study is notably higher than those in other studies. This disparity can be attributed to differences in the dynamic range, environment, and clustering parameters and dimensions that were considered. For example, [39] and [14] considered time clusters and spatial clusters, respectively, excluding the separation of paths in other dimensions hence resulting in fewer clusters. LOS links are also found to have a slightly greater number of clusters compared to NLOS links considered in this study. In addition, Table V shows the maximum number of clusters $\max(N_{\mathrm{C}})$ and distinct objects $\max(N_{\mathrm{O}})$ across the links in both environments. It can be observed that the indoor case has links that have more than twice N_{C} or N_{O} compared to the outdoor case.

TABLE V
STATISTICAL SUMMARY OF THE NUMBER OF CLUSTERS AND OBJECTS ACROSS THE LINKS

Scenario	Reference	Link type	$\mu_{N_{\mathrm{C}}}$	$\sigma_{N_{\mathrm{C}}}$	max N_{C}	max N_{O}
Indoor hall	This study	LOS	13.6	4.7	22	12
		NLOS	9.5	6.1	27	12
Indoor hotspot–office	Table III of [39]	LOS	1.9	1.3	N/A	N/A
		NLOS	2.8	1.7	N/A	N/A
Urban micro	This study	LOS	4.5	3.3	12	4
		NLOS	2.3	2.1	5	4
Urban micro	Section III-A of [14]	LOS	0.7	N/A	N/A	N/A
		NLOS	1.8	N/A	N/A	N/A

V. CONCLUSION

This article presented the analysis of wave interaction with various objects in an indoor and outdoor scenario at 142 GHz. The MBRL was improved in terms of computational speeds and was utilized to estimate the propagation path trajectory of MPCs obtained from single-directional measurements up to fourth-order reflections. For LOS links, about 80% of the power can be attributed to the direct path. As for NLOS links, the first and second-order reflections constitute about 60% of the total power. Furthermore, propagation paths reflected on large objects such as walls generally have the most share of the total received power in each link, followed by those on the floor and ceiling. The finding supports the importance of 3-D models and analyses of the sites. Meanwhile, small objects can contribute up to about half of the total received power in a link. Typical reflection losses of each object depended more on its shape and structure than its material composition. The visibility distance of each object was mainly influenced by its size and blockage from the surrounding objects. In addition, the number of multipath clusters on large objects is roughly four times and two times more than small objects in the studied indoor and outdoor scenarios, respectively. While only a fraction of clusters are typically formed on small objects, there are some links where they can generate up to four clusters. Up to fourth-order reflections are found in the small-cell sub-THz indoor and outdoor channels. Separate modeling of large and

small objects would enhance the geometry-based modeling of channels, especially for radio localization applications.

ACKNOWLEDGMENT

The authors acknowledge the computational resources provided by the Aalto Science-IT Project. They would like to thank Joona Vehkalahti, Hassan Muhammad, and Xue Bing for their assistance during the channel measurements.

REFERENCES

[1] H. Wymeersch et al., "Integration of communication and sensing in 6G: A joint industrial and academic perspective," in *Proc. IEEE 32nd Annu. Int. Symp. Pers., Indoor Mobile Radio Commun. (PIMRC)*, Sep. 2021, pp. 1–7.

[2] S. L. H. Nguyen, J. Järveläinen, A. Karttunen, K. Haneda, and J. Putkonen, "Comparing radio propagation channels between 28 and 140 GHz bands in a shopping mall," in *Proc. 12th Eur. Conf. Antennas Propag. (EuCAP)*, Apr. 2018, pp. 1–5.

[3] Y. Xing, O. Kanhere, S. Ju, and T. S. Rappaport, "Indoor wireless channel properties at millimeter wave and sub-terahertz frequencies," in *Proc. IEEE Global Commun. Conf. (GLOBECOM)*, Dec. 2019, pp. 1–6.

[4] B.-E. Olsson, C. Larsson, M. N. Johansson, and S. L. H. Nguyen, "Radio propagation in an office environment at 140 GHz and 28 GHz," in *Proc. 15th Eur. Conf. Antennas Propag. (EuCAP)*, Mar. 2021, pp. 1–5.

[5] J. Gomez-Ponce et al., "Impact of common reflecting and absorbing building materials on THz multipath channels," *Radio Sci.*, vol. 57, no. 2, Feb. 2022.

[6] C. Larsson, B.-E. Olsson, S. L. H. Nguyen, and M. Johansson, "Propagation measurements comparing indoor and outdoor hotspot coverage at 28, 58, and 143 GHz," in *Proc. 16th Eur. Conf. Antennas Propag. (EuCAP)*, Mar. 2022, pp. 1–5.

[7] B. De Beelde, E. Tanghe, D. Plets, and W. Joseph, "Indoor radio channel modeling at D-band frequencies," in *Proc. 16th Eur. Conf. Antennas Propag. (EuCAP)*, Mar. 2022, pp. 1–4.

[8] A. Nimr, Ed., "Deliverable D2.3 radio models and enabling techniques towards ultra-high data rate links and capacity in 6G," Hexa-X Project, Tech. Rep., 2023. [Online]. Available: https://hexa-x.eu/deliverables/

[9] J. P. Kermoal, L. Schumacher, K. I. Pedersen, P. E. Mogensen, and F. Frederiksen, "A stochastic MIMO radio channel model with experimental validation," *IEEE J. Sel. Areas Commun.*, vol. 20, no. 6, pp. 1211–1226, Aug. 2002.

[10] A. A. M. Saleh and R. Valenzuela, "A statistical model for indoor multipath propagation," *IEEE J. Sel. Areas Commun.*, vol. SAC-5, no. 2, pp. 128–137, Feb. 1987.

[11] "5G; study on channel model for frequencies from 0.5 to 100 GHz," Eur. Telecommun. Standards Inst., Tech. Rep. 39.901, 2022. [Online]. Available: https://www.etsi.org/

[12] L. Liu et al., "The COST 2100 MIMO channel model," *IEEE Wireless Commun.*, vol. 19, no. 6, pp. 92–99, Dec. 2012.

[13] C. Sturm, W. Sorgel, T. Kayser, and W. Wiesbeck, "Deterministic UWB wave propagation modeling for localization applications based on 3D ray tracing," in *IEEE MTT-S Int. Microw. Symp. Dig.*, Jun. 2006, pp. 2003–2006.

[14] S. Ju and T. S. Rappaport, "Sub-terahertz spatial statistical MIMO channel model for urban microcells at 142 GHz," in *Proc. IEEE Global Commun. Conf. (GLOBECOM)*, Dec. 2021, pp. 1–6.

[15] P. Kyösti, M. F. De Guzman, K. Haneda, N. Tervo, and A. Pärssinen, "How many beams does sub-THz channel support?" *IEEE Antennas Wireless Propag. Lett.*, vol. 21, no. 1, pp. 74–78, Jan. 2022.

[16] B. De Beelde, D. Plets, C. Desset, E. Tanghe, A. Bourdoux, and W. Joseph, "Material characterization and radio channel modeling at D-band frequencies," *IEEE Access*, vol. 9, pp. 153528–153539, 2021.

[17] M. A. Aliouane, J.-M. Conrat, J.-C. Cousin, and X. Begaud, "Material reflection measurements in centimeter and millimeter wave ranges for 6G wireless communications," in *Proc. Joint Eur. Conf. Netw. Commun. 6G Summit (EuCNC/6G Summit)*, Jun. 2022, pp. 43–48.

[18] M. Jacob, T. Kürner, R. Geise, and R. Piesiewicz, "Reflection and transmission properties of building materials in D-band for modeling future mm-wave communication systems," in *Proc. 4th Eur. Conf. Antennas Propag.*, Apr. 2010, pp. 1–5.

[19] M. Zhu and F. Tufvesson, "Virtual multi-link propagation investigation of an outdoor scenario at 300 MHz," in *Proc. 7th Eur. Conf. Antennas Propag. (EuCAP)*, Apr. 2013, pp. 687–691.

[20] M. Ghoraishi, J. Takada, and T. Imai, "Identification of scattering objects in microcell urban mobile propagation channel," *IEEE Trans. Antennas Propag.*, vol. 54, no. 11, pp. 3473–3480, Nov. 2006.

[21] P. Koivumäki, A. Karttunen, and K. Haneda, "Wave scatterer localization in outdoor-to-indoor channels at 4 and 14 GHz," in *Proc. 16th Eur. Conf. Antennas Propag. (EuCAP)*, Mar. 2022, pp. 1–5.

[22] J. Poutanen, K. Haneda, J. Salmi, V.-M. Kolmonen, F. Tufvesson, and P. Vainikainen, "Analysis of radio wave scattering processes for indoor MIMO channel models," in *Proc. IEEE 20th Int. Symp. Pers., Indoor Mobile Radio Commun.*, Sep. 2009, pp. 102–106.

[23] K. Belbase, M. Kim, and J.-I. Takada, "Study of propagation mechanisms and identification of scattering objects in indoor multipath channels at 11 GHz," in *Proc. 9th Eur. Conf. Antennas Propag. (EuCAP)*, Apr. 2015, pp. 1–4.

[24] M. D. Baldé, B. Uguen, A. Karttunen, and K. Haneda, "Identification of wave scatterers in an urban MicroCellular environment at 32 GHz," in *Proc. IEEE 29th Annu. Int. Symp. Pers., Indoor Mobile Radio Commun. (PIMRC)*, Sep. 2018, pp. 1400–1404.

[25] J. Poutanen, K. Haneda, L. Liu, C. Oestges, F. Tufvesson, and P. Vainikainen, "Parameterization of the COST 2100 MIMO channel model in indoor scenarios," in *Proc. 5th Eur. Conf. Antennas Propag. (EUCAP)*, Apr. 2011, pp. 3606–3610.

[26] M. Zhu, G. Eriksson, and F. Tufvesson, "The COST 2100 channel model: Parameterization and validation based on outdoor MIMO measurements at 300 MHz," *IEEE Trans. Wireless Commun.*, vol. 12, no. 2, pp. 888–897, Feb. 2013.

[27] A. Karttunen, J. Jarvelainen, A. Khatun, and K. Haneda, "Radio propagation measurements and WINNER II parameterization for a shopping mall at 60 GHz," in *Proc. IEEE 81st Veh. Technol. Conf. (VTC Spring)*, May 2015, pp. 1–5.

[28] N. A. Abbasi et al., "Double-directional channel measurements for urban THz communications on a linear route," in *Proc. IEEE Int. Conf. Commun. Workshops (ICC Workshops)*, Jun. 2021, pp. 1–6.

[29] A. Kakkavas, M. H. C. García, G. Seco-Granados, H. Wymeersch, R. A. Stirling-Gallacher, and J. A. Nossek, "Position information from reflecting surfaces," *IEEE Wireless Commun. Lett.*, vol. 10, no. 6, pp. 1300–1304, Jun. 2021.

[30] M. Zhu, A. Singh, and F. Tufvesson, "Measurement based ray launching for analysis of outdoor propagation," in *Proc. 6th Eur. Conf. Antennas Propag. (EUCAP)*, Mar. 2012, pp. 3332–3336.

[31] M. F. De Guzman, P. Koivumäki, and K. Haneda, "Double-directional multipath data at 140 GHz derived from measurement-based ray-launcher," in *Proc. IEEE 95th Veh. Technol. Conf. (VTC-Spring)*, Jun. 2022, pp. 1–6.

[32] P. Koivumäki, G. Steinböck, and K. Haneda, "Impacts of point cloud modeling on the accuracy of ray-based multipath propagation simulations," *IEEE Trans. Antennas Propag.*, vol. 69, no. 8, pp. 4737–4747, Aug. 2021.

[33] P. Koivumäki and K. Haneda, "Point cloud ray-launching simulations of indoor multipath channels at 60 GHz," in *Proc. IEEE 33rd Annu. Int. Symp. Pers., Indoor Mobile Radio Commun. (PIMRC)*, Sep. 2022, pp. 1–7.

[34] J. Amanatides and A. Woo, "A fast voxel traversal algorithm for ray tracing," *Eurographics*, vol. 87, no. 3, pp. 3–10, 1987.

[35] M. F. De Guzman, M. Hassan, and K. Haneda, "Uncertainty of millimeter-wave channel sounder due to integration of frequency converters," in *Proc. 17th Int. Symp. Wireless Commun. Syst. (ISWCS)*, Sep. 2021, pp. 1–6.

[36] K. Haneda, S. L. H. Nguyen, J. Järveläinen, and J. Putkonen, "Estimating the omni-directional pathloss from directional channel sounding," in *Proc. 10th Eur. Conf. Antennas Propag. (EuCAP)*, Apr. 2016, pp. 1–5.

[37] S. L. H. Nguyen, K. Haneda, and J. Putkonen, "Dual-band multipath cluster analysis of small-cell backhaul channels in an urban street environment," in *Proc. IEEE Globecom Workshops (GC Wkshps)*, Dec. 2016, pp. 1–6.

[38] N. Czink et al., "Automatic clustering of MIMO channel parameters using the multi-path component distance measure," Tech. Rep., Jan. 2005.

[39] Y. Xing, T. S. Rappaport, and A. Ghosh, "Millimeter wave and sub-THz indoor radio propagation channel measurements, models, and comparisons in an office environment," *IEEE Commun. Lett.*, vol. 25, no. 10, pp. 3151–3155, Oct. 2021.

Mar Francis De Guzman (Graduate Student Member, IEEE) received the B.S. degree in electronics and communications engineering and the M.S. degree in electrical engineering from the University of the Philippines Diliman, Quezon City, Philippines, in 2015 and 2017, respectively. He is currently pursuing the D.Sc. degree in technology with the School of Electrical Engineering, Aalto University, Espoo, Finland.

In 2023, he was a Visiting Doctoral Student at the Centre for Wireless Communications, University of Oulu, Oulu, Finland. His research interests include radio channel measurements, simulations, and modeling for 6G wireless communication systems.

Katsuyuki Haneda (Member, IEEE) is an Associate Professor with the School of Electrical Engineering, Aalto University, Espoo, Finland. His current research interests include high-frequency radios such as millimeter-wave and beyond and wireless for medical and smart-city applications.

Dr. Haneda was the author and coauthor of several best paper and student paper awards at the IEEE Vehicular Technology Conference and European Conference on Antennas and Propagation, among others. He received the R. W. P. King Paper Award from IEEE TRANSACTIONS ON ANTENNAS AND PROPAGATION in 2021, together with Dr. Usman Virk. He was the Co-Chair of a disciplinary working group on radio channels in European COST Actions CA15104 Inclusive Radio Communication Networks for 5G and Beyond (IRACON) between 2016 and 2020. He is the Technical Program Committee Co-Chair of the 17th European Conference on Antennas and Propagation (EuCAP 2023), Florence, Italy. He was an Associate Editor of IEEE TRANSACTIONS ON ANTENNAS AND PROPAGATION between 2012 and 2016 and an Editor of IEEE TRANSACTIONS ON WIRELESS COMMUNICATIONS between 2013 and 2018. He was a Guest Editor of a Special Issue on "Antennas and Propagation Aspects of In-Band Full-Duplex Applications and on Artificial Intelligence in Radio Propagation for Communications" from IEEE TRANSACTIONS ON ANTENNAS AND PROPAGATION in 2021 and 2022, respectively.